International Journal of Thermal Sciences 49 (2010) 769–785

Contents lists available at ScienceDirect

International Journal of Thermal Sciences

journal homepage: www.elsevier.com/locate/ijts

Heat transfer of a radially rotating furrowed channel with two opposite skewed sinusoidal wavy walls

S.W. Chang [a,*], A.W. Lees [b,1], T.-M. Liou [c], G.F. Hong [d,2]

[a] Thermal Fluids Laboratory, National Kaohsiung Marine University, No. 142, Haijhuan Road, Nanzih District, Kaohsiung City 81143, Taiwan, ROC
[b] School of Engineering, Swansea University, Singleton Park, Swansea, South Wales SA2 8PP, UK
[c] Department of Power Mechanical Engineering, National Tsing Hua University, 30013 Hsinchu, Taiwan, ROC
[d] Department of Marine Engineering, National Kaohsiung Marine University, No. 142, Haijhuan Road, Nanzih District, Kaohsiung City 81143, Taiwan, ROC

ARTICLE INFO

Article history:
Received 23 May 2009
Received in revised form
30 September 2009
Accepted 24 November 2009
Available online 16 December 2009

Keywords:
Turbine rotor blade cooling
Rotating heat transfer
Skew wavy roughness

ABSTRACT

An experimental study of heat transfer in a radially rotating furrowed channel with two opposite walls enhanced by skewed sinusoidal waves was performed to generate the full-field Nusselt number (Nu) data over two wavy walls. Although the static wavy channel has been proven as an effective heat transfer enhancement (HTE) measure, no previous study examined its heat transfer performances with rotation. As another first-time attempt for turbine cooling researches, the Nu scans over the entire rotational leading (stable) and trailing (unstable) walls were acquired using the infra-red thermography which proved highly advantageous due to its capability to examine the rotating buoyancy effects in details. A selection of experimental data illustrates the full-field Nu variations responding to the changes of Reynolds (Re), rotation (Ro) and buoyancy (Bu) numbers. Parametric analysis is subsequently followed to disclose the individual and interdependent Re, Ro and Bu effects on Nu in the attempt to derive the heat transfer correlations for the area-averaged Nu over the developed flow region ($\overline{Nu}_{FD}$) on the rotational leading and trailing wavy walls. Within the parametric ranges tested, the rotational leading and trailing $\overline{Nu}_{FD}$ values respectively fall between 3.4–4.3 and 4.2–6.4 times of the Dittus–Boelter datum, which grant the potential applicability of wavy channel as a HTE measure for cooling of gas turbine rotor blades.

1. Introduction

It is highly desirable to increase turbine entry temperatures of gas turbine engines to about 1800–2000 K, so gaining thermodynamic advantages resulting in improved fuel economy. The coolant passages inside the turbine rotor blade play a crucial role in assuring the structural integrity and life span of the turbine blade. Surface ribs, dimples and pin-fins are widely used to facilitate heat transfer enhancements (HTE) for these coolant passages. As a result, a large number of heat transfer research studies have incorporated these HTE devices with the simulated, but simplified, coolant passages of the rotor blade to examine their heat transfer performances under rotating conditions. In general, the indicative HTE characteristics developed in the stationary channels are retained in the likewise rotating channels, but their HTE effects can be either locally amplified or moderated due to the interdependent effects of Coriolis forces and rotating buoyancy. Such rotation induced HTE modifications depend on the geometries of HTE devices, the shape and orientation of the rotating channel, the flow direction relative to the rotation and the thermal boundary conditions [1–13]. With steady-state operations, the rotation manifesting influences on HTE performances originate from the well known Coriolis and centrifugal accelerations. These rotation induced body forces affect the in-duct Poiseuille-like flow and interact with the surface roughness to produce rich modes of flow structures inside a rotating passage. As the rotation of turbine rotor blades is perpendicular to the plane of main shear, the Coriolis forces affect both mean flow and turbulent fluctuations considerably. Depending on the channel shape, the Coriolis secondary flows can be established to drive the cool fluids from the channel core toward the unstable wall with the heated fluids returned to the stable wall after washing the peripheries of a rotating channel. Additionally, as the turbulence productions for channel flows are mainly triggered by the momentum exchange through intensive interactions between the fluctuating streamwise and cross-stream velocities, the turbulent activities are augmented when the Coriolis forces act in tandem with these events but are attenuated when the

* Corresponding author. Tel.: +886 7 8100888 5216; fax: +886 7 571 60 13.
E-mail addresses: swchang@mail.nkmu.edu.tw (S.W. Chang), A.W.Lees@swansea.ac.uk (A.W. Lees), tmliou@pme.nthu.edu.tw (T.-M. Liou), tsuchien@hotmail.com (G.F. Hong).
[1] Tel.: +44 1792 205678.
[2] Tel.: +886 7 8100888 5217.

1290-0729/$ – see front matter © 2009 Elsevier Masson SAS. All rights reserved.
doi:10.1016/j.ijthermalsci.2009.11.011

Nomenclature

English symbols

a	amplitude of wall-wave (m)
Bu	Buoyancy number $= Ro^2\beta(T_w - T_b)(R/d)$
d	hydraulic diameter of the test channel (m)
H	channel height (m)
k_f	Thermal conductivity of fluid (W m^{-1} K^{-1})
L	channel length (m)
Nu	local Nusselt number $= q_f d/k_f (T_w - T_b)$
$\overline{Nu}$	area-averaged Nu for periodically developed flow region
Nu_0	local Nusselt number at zero rotational speed
Nu_∞	Nusselt number value evaluated from Dittus–Boelter correlation
Pr	Prandtl number $= \mu C_p/k$
q_f	convective heat flux (W m^{-2})
R	rotating radius at mid-span of test duct from rotating axis (m)
Re	Reynolds number $= \rho W_m d/\mu$
Ro	Rotating number $= \Omega d/W_m$
S	channel peripheral length (m)
T_b	fluid bulk temperature (K)
T_w	wall temperature (K)
T_∞	ambient temperature (K)
W	channel width (m)
W_m	mean flow velocity (m s^{-1})
x, y	axial and spanwise coordinates (m)
X,Y	dimensionless coordinates ($=x/d, y/d$)

Greek symbols

α	attack angle of wall-waves ($=45^\circ$)
β	Thermal expansion coefficient of fluid (K^{-1})
ρ	density of fluid (kg m^{-3})
λ	wave pitch (m)
μ	fluid dynamic viscosity (kg m^{-1} s^{-1})
Ω	rotational speed of test duct (rad s^{-1})
$\Psi, \varphi_1, \varphi_2$	unknown functions

Subscripts

FD	fully developed flow
0	refers to non-rotating situation

two act in opposition [14]. This type of turbulent interactions leads to another persistent Coriolis effects on turbulent flows which respectively stabilize and destabilize the turbulent fluctuations at the stable and unstable walls of a rotating channel, even if the various flow mechanisms triggered by different HTE devices prevail over the entire rotating channel. By increasing the rate of rotation further, the large scale roll-cells start emerging over the cross-sectional plane of a rotating channel due to the Taylor–Görtler instabilities [15,16]. These large scale roll-cell vortices emerging at high rotation rates in the smooth-walled rotating channels [15,16] are also found in numerical simulations near the stable wall of the rotating rib-roughened channel [17], which can lead to the heat transfer elevations from the static references on the stable walls at high rotation numbers ($Ro > 0.6$) [9–12]. Nevertheless, due to the Coriolis effects on mean flows and turbulent activities, peripheral heat transfer differences between the stable and unstable walls of the rotating channels are consistently observed [1–13,17]. While the vortical interactions between the secondary flows induced by Coriolis forces and surface ribs affect the local HTE performances in a rotating rib-roughened channel, the developments of Coriolis and ribwise secondary flows are closely controlled by the sectional perimeters of the rotating channel that confine the developments of these secondary flows. By way of varying the sectional shape of the non-circular rotating channel in respect to its axis of rotation, the flow structures and their HTE performances are modified. Local HTE performances in the rotating channels are dependent on the shape [1], the aspect ratio [13] and the orientation [5,9] of a rotating channel. For rotating pin-fin channels fitted with pin-fins, which serve as another mainstream of HTE devices as a part of internal cooling network at the trailing edge of a rotor blade, the Coriolis secondary flows are constantly disturbed by these pin-fins. But the Coriolis and rotating buoyancy forces still prevail over a rotating pin-fin channel that results in the aforementioned heat transfer differences between their stable and unstable walls [12]. Clearly, the flow features generated by various HTE devices such as ribs, pin-fins and dimples, which interact with the rotation forces, produce different cooling performances inside these enhanced rotating channels. The different HTE performances for the rotating channels fitted with surface ribs, dimples and pin-fins are revealed in [12] by comparatively examining the variations of Nu/Nu_∞ against Ro where Nu_∞ is evaluated from the Dittus–Boelter correlation. Among the rotating channels with smooth-wall, 90° and 45° ribs, surface dimples and pin-fins, the smooth channel exhibits the lowest Nu/Nu_∞ but with the largest rotational impacts. The endwall Nu/Nu_∞ ratios for the rotating pin-fin channels are compatible with those in the dimpled channel but are lesser than those in the duct roughened by 45° ribs. Lesser extents of Coriolis effects on the endwall heat transfer performances due to the presence of pin-fin array are observed in the rotating pin-fin channel [12].

Another influence in a rotating channel is the centrifugal acceleration that can be up to 10^5 g in a turbine rotor blade. With the prevailing fluid temperature differences in the flow as a result of heat convection, the interactions between centrifugal acceleration and the density gradients of the fluids inside a heated rotating channel differentiate the centrifugal body forces from the hydrostatic to the hydrodynamic states and this drives the less dense (warmer) fluids toward the axis of rotation. This mechanism, referred to as the rotating buoyancy effect, depends markedly on the streamwise and spanwise temperature gradients of the coolant flow and provides different effects on heat transfer for radial outward and inward flows following the analogies to the mixing convections with counter and parallel flow conditions [18,19]. Although the simple analogy of mixed convection could offer an interpretation on the rotating buoyancy effect discovered for rotating channels [19], the earlier study [20] has demonstrated that the rotating buoyancy effect depends on other controlling flow parameters (such as Ro) that can either enhance or impair heat transfer in a rotating smooth-walled channel. With rotating channels fitted with various HTE devices, the variations of fluid temperatures form an intricate and extremely complicated buoyancy interaction. This rotating buoyancy effect is later treated as the aiding and opposing flows with the effect of rotating buoyancy to be concluded as the increase and decrease of both the wall shear stress and the heat transfer rate for the buoyancy induced aiding and opposing flows respectively [21,22]. These numerical results indicate the complex and inter-correlative natures of the rotating buoyancy and Coriolis secondary flows that interact with the surface ribs and the sharp 180° turn [21,22] for multipass rib-roughened channels. However, the presence of surface ribs considerably suppresses the influence of rotating buoyancy on heat

transfer from the smooth-walled conditions [23] where the rib induced agitated flows are absent. Due to the lack of full-surface heat transfer measurements collected from the rotating channels with prescribed buoyancy levels and the various rotating buoyancy effects reported to date, the impacts of rotating buoyancy on heat transfer still remain as puzzles; even if it is now clear that the rotating buoyancy effects deem to be *Re*, *Ro* and location dependent. To clarify the detailed influences of rotating buoyancy effect, in particular over the enhanced rotating surfaces with potential cooling applications to gas turbine rotor blades, it is crucially important to employ a technique that enables the measurements of full-surface Nusselt number (*Nu*) distributions at various buoyancy levels. Whilst the experimental method for measuring the full *Nu* scans over the rotating surface with the buoyancy effect considered is under investigation, the search for HTE surfaces for turbine rotor blade cooling develops at a good pace. In this respect, the HTE effects attributed to the deepened scales [24] and the compound roughness of V-ribs and scales [25] were previously investigated. Although their considerable HTE effects in the rotating channel were realized [24,25], the pressure drop penalties were accordingly generated due to the enhanced turbulences, friction drags and flow separations [26]. As the wavy channels facilitate considerable HTE effects with relatively low pressure drops, the wavy channels propose their potential cooling applications to turbine rotor blades. The macroscopic mixings between the near wall and core fluids triggered by the shear layer instability and the self-sustained oscillations [27–29]; along with the secondary flows induced by the skewed sinusoidal walls [30] offers considerable HTE impacts. Despite of the potentials for blade cooling applications, no heat transfer result is available for a rotating wavy channel to date.

To obtain the full *Nu* scan over rotating channels, the naphthalene sublimation method and the transient/steady-state liquid crystal thermometry [8,9,13,31,32] have been previously applied. But none of these studies can successfully reveal the rotating buoyancy effects. The *Nu* data acquired by naphthalene sublimation method simulates the zero-buoyancy condition. The transient liquid crystal thermometry (TLCT) employs the ***heated*** flow over the ***cold*** rotating surface that creates the inverse buoyancy condition from the actual blade cooling scenario. The thermal boundary layers over the ***heated*** surface during the period of data acquisition using TLCT are under developing. With steady-state liquid crystal (LC) techniques, the small sensitivity temperature range for the LC prohibits the full coverage of wall temperatures over a rotating surface at the buoyancy levels representative to engine conditions. A number of heat fluxes are used to shift the "isotherms" at the specific sensitivity temperature of the LC over the entire heated surface in order to compose a full *Nu* scan that results in various rotating buoyancy levels in each *Nu* scan. To resolve these difficulties, the surface temperatures over the rotating heated wall for this study are detected by means of infra-red thermography which can capture the full-surface wall temperatures at the pre-defined heating conditions. The pressing need to devise an experimental method that enables the acquisition of full *Nu* scans including the rotating buoyancy effects, together with the lack of heat transfer data for rotating wavy channels, motivate the present investigation to examine the Coriolis and rotating buoyancy effects on the heat transfer performance of a rotating wavy channel using the infra-red thermography. To the best of the authors' knowledge, no previous approach can successfully provide the full *Nu* scans over a rotating surface with the buoyancy effects examined, nor is the *Nu* data for a rotating wavy channel ever reported in the open literature. This experimental study detects the full *Nu* scans from a radially rotating furrowed channel with two opposite walls roughened by skewed sinusoidal waves. Area-averaged *Nu* data for the developed flow region ($\overline{Nu}_{FD}$) over the leading and trailing rotating wavy walls have been generated and analyzed. Parametric heat transfer variations in association with the individual and interactive effects of *Re*, *Ro* and *Bu* are subsequently illustrated during which the empirical heat transfer correlation for $\overline{Nu}_{FD}$ is developing. A set of $\overline{Nu}_{FD}$ correlations is derived that permits the isolated and/or interdependent *Ro* and *Bu* effects on $\overline{Nu}_{FD}$ to be quantified. This research approach which generates the full *Nu* scans with the capability to analyze the rotating buoyancy effect is applicable to other channel geometries.

2. Experimental facilities

2.1. Rotating apparatus

The surface temperatures over the rotating wavy wall are detected by means of infra-red thermography at a set of pre-defined test conditions with specific buoyancy levels. The maximum acceleration sustainable by this type of IR is 10 g, which converts to the maximum rotational speed of 120 rev/min for the present test apparatus. The rotating rig and the test section are designed and constructed to permit the high pressure tests in order to extend the *Ro* range by increasing the fluid density due to pressurization. As shown in Fig. 1, the rotating rig comprises a rotating platform on which the assorted simulated blade cooling passages can be mounted and tested, the rotating arm to which the infra-red (IR) camera is secured and the units of coolant supply, power supply and signal transmission. The rotor assembly consists of two hollow shafts (1)(2) connected to a rotating test platform (3), which is supported by two main bearings (4). The test module (5) is mounted on the rotating test platform (3) with the mean rotating radius (*R*) to the mid-span of the test section of 400 mm which is equivalent to 17 hydraulic diameters of the test channel. Each hollow shaft (1)(2) has a centrally located blind bore to permit pressurized air entering the shaft via the water cooled high pressure rotary seal (6). The pressurized airflow enters the rotor and passes through the test section that exits through an exhaust valve (7) at the exit of the convergent chamber (8) to pressurize the entire flow system. The test pressures in the test channel are controlled by adjusting the exhaust valve (7). For this set of experiments, the pressures are in the range of 2.2–4 bars which enable the *Re* and *Ro* ranges of 4000–14000 and 0–0.22 respectively. This rotor assembly is driven by a variable-speed DC motor (9) via a pulley system using three V belts. The electrical powers for heating the test module (5) and the IR camera (10) are individually transmitted to the rotor by means of 2 units of power slip rings (11) (12). Two instrumentation slip ring units (13)(14) respectively transfer the electrical signals from the thermocouples measuring the fluid temperatures at the entry and exit of the test section via the Fluke Net-Daq 2640A data logger and from the IR camera to the computer for temperature scan, data storage and processing. The rotor speed is measured by an optical pick-up and encoder unit (15) attached to the shaft (2). The rotor assembly is dynamically balanced by the counter weight (16)(17) secured respectively on the back of the rotating platform and the opposite rotating arm with IR camera.

2.2. Heat transfer test module

The heat transfer test module with airflow in the radially outward direction is shown as (5) in Fig. 1-a with more enlarged details in Fig. 1-b. As shown in Fig. 1-b, the airflow enters the entry plenum chamber (1) in which the meshes and honeycomb are installed to straighten the flow. The entry plenum chamber is connected with the Teflon entry flange (2) through which the flow passage at the flange central matches exactly the contour of the

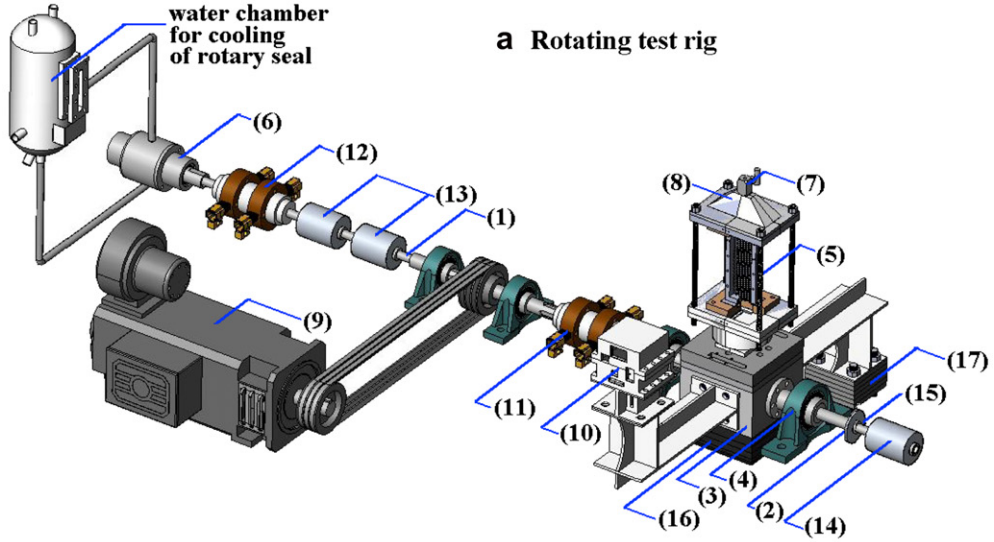

(1)(2) Hollow shaft
(3) Rotating platform
(4) Main bearing
(5) Test module
(6) Rotary seal
(7) Exhaust valve
(8) Convergent chamber
(9) Variable speed motor
(10) IR camera
(11)(12) Power slip ring
(13)(14) Instrumentation slip ring
(15) Optical speed dector
(16)(17) Balance weight

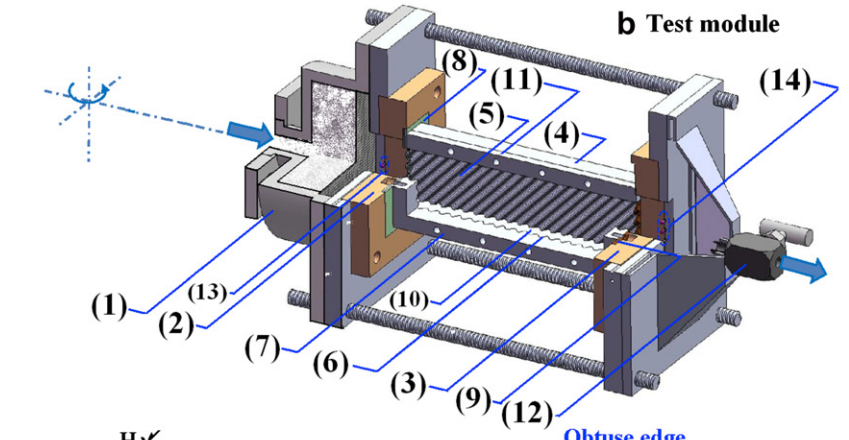

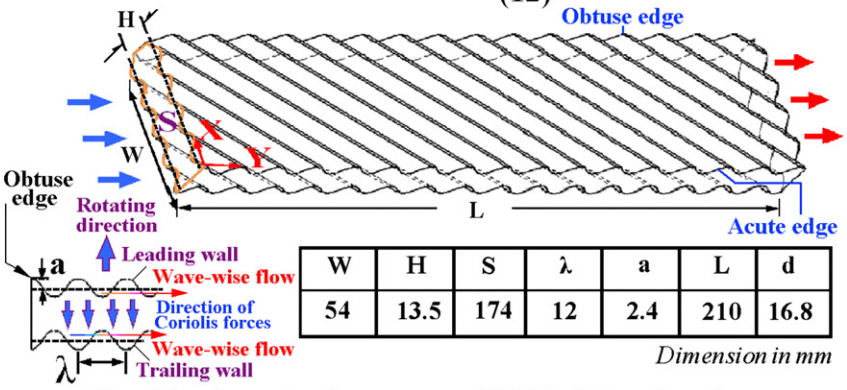

W	H	S	λ	a	L	d
54	13.5	174	12	2.4	210	16.8

Dimension in mm

(1) Entry plenum chamber
(2) Teflon entry flange
(3) Teflon exit flange
(4) Teflon wavy back wall
(5)(6) Stainless steel heating/wavy foils
(7) Front Teflon frame
(8)(9) Two-piece copper plates
(10)(11) Teflon sidewalls
(12) Exit plenum chamber
(13) Thermocouple measuring fluid entry temperature
(14) Thermocouples measuring fluid exit temperatures

Fig. 1. Experimental facilities (a) rotating rig, (b) heat transfer test module.

cross-section of the furrowed channel with two opposite walls enhanced by the skewed waves. The area ratio between the entry plenum (1) and the test section is about 4, which creates the abrupt flow entry condition. Due to the sharp flow entrance, the hydraulic boundary layers are re-developed at the immediate flow entrance of the test channel. Between the Teflon entry (2) and exit (3) flanges, a 30 mm thick Teflon wavy back wall (4) is installed. A pair of 0.1 mm thick stainless steel foils of 54 mm in width (W) and 194 mm in length (L) is forged to form the wavy heating foils (5)(6) with skewed sinusoidal waves. As indicated in Fig. 1-b, the amplitude (a) and the wave pitch (λ) for the wall waviness are 2.4 mm and 12 mm respectively, which define the sinusoidal waviness with the amplitude-to-pitch ratio of 0.2. The peripheral length of the cross-section (S) for the skewed wavy channel is 174 mm which gives the hydraulic diameters (d) of the wavy channel of 16.8 mm. This channel hydraulic diameter is selected as the characteristic lengths to define Nu, Re, Ro and Bu. The wavy heating foils (5) and (6) are respectively attached on the Teflon wavy back wall (4) and secured by the front Teflon frame (7) to allow the optical assessment of wall temperature (T_w) measurements over this wavy foil (6). As indicated in Fig. 1-b, the leading and trailing walls correspond respectively the stable and unstable sides for this rotating channel. By changing the direction of rotation, this heating wavy foil (6) provides T_w information on the leading and trailing walls of the rotating channel. The detailed T_w measurements over the wavy heating foil (6) for each test condition are imaged by the calibrated two-dimensional infra-red camera which takes 0.01 s to complete a 239 × 255 matrix scan. The back surface of the wavy heating foil (6) is painted black to increase its emission. Each end of the heating foils (5)(6) is squeezed between the two-piece entry (8) or exit (9) copper plates which are respectively sandwiched between the flow entry/exit flanges (2)(3) and the back/front Teflon walls (4)(7). Two Teflon channel side-walls (11)(12) with the waviness to fit the front and back wavy foils (5)(6) set the channel height (H) of 13.5 mm, which gives the channel aspect ratio (W/H) of 4. The complete electrical circuit for the heating power is connected in series with two copper plates (8)(9) connecting the electrical cables and secured on the entry and exit flanges (2)(3). The adjustable and basically uniform heat flux over each wavy stainless steel heating foil is accordingly generated. A convergent exit plenum chamber (12) is fitted between the exit of the wavy channel and the exhaust valve. Components (1)–(12) are tightened by four draw bolts through four positioning holes on the entry and exit flanges (2)(3). The X–Y coordinate system adopted here is also indicated in Fig. 1-b with its origin positioned at the lower entry corner of the wavy channel. A K-type thermocouple (13) is positioned at the geometric center of the flow entry section and sandwiched between the entry plenum chamber (1) and the flange (2) to detect the fluid entry temperature. With the similar mechanical layout at the flow exit, three X-wise K-type thermocouples (14) alongside the centerline of the flow exit are positioned with equal intervals to measure the fluid exit temperatures. The measured fluid exit temperature for each test condition is obtained by averaging these three temperature measurements detected from the thermocouples (14).

As depicted in Fig. 1-b, the two opposite wavy surfaces of the wavy channel are arranged as the in-line manner to form the furrowed channel and characterized by the four dimensionless geometric parameters of:

Channel length (L) to channel width (W) ratio of 194 mm/54 mm = 3.6
Channel width (W) to channel height (H) ratio of 54 mm/13.5 mm = 4
Wave amplitude (a) to channel height (H) ratio of 2.4 mm/13.5 mm = 0.178
Wave amplitude (a) to pitch (λ) ratio of 2.4 mm/12 mm = 0.2
The angles of attack for the skewed wavy = 45°.

3. Experimental program and data reduction

3.1. Program

It is now widely accepted that the Reynolds (Re) and rotation (Ro) numbers respectively characterize the inertial and Coriolis force effects in their own rights with the levels of rotating buoyancy to be indexed by buoyancy number (Bu). The rotating buoyancy effects for turbine rotor blade cooling cannot be overlooked due to the extremely high centrifugal forces encountered by the airflows circulating inside the coolant passages of a turbine rotor blade. The density ratio ($\Delta\rho/\rho$) in terms of $\beta(T_w - T_b)$ coupled with the centrifugal acceleration defines the buoyancy number (Bu) in the form of $\beta(T_w - T_b)Ro^2(R/d)$ which physically reflects the relative strength of rotating buoyancy force to flow inertial force. This experimental study is formulated to parametrically examine the heat transfer performances in association with the controlling dimensionless parameters that affect the local Nusselt numbers (Nu) over the rotating wavy walls. Variations in each governing dimensionless parameter such as Re, Ro, Pr or Bu for a set of predefined geometric and thermal boundary conditions result in corresponding Nu variations. The functional relationships between Nu and the governing dimensionless parameters can be revealed by analyzing the Nu variations corresponding to the systematic variations of each flow parameter. With the present T_b range of 305–347 K, the maximum variation in Prandtl number (Pr) of the tested coolant is negligible about 1.4%, hence the Pr effect on Nu is not investigated. This parametric study attempts to determine the functional relationships between Nu and Re, Ro and Bu for the predefined geometric and thermal boundary conditions simulated by the test section described in Fig. 1-b in the form of

$$Nu = \Psi\{Re, Ro, Bu,\ X, \text{geometric and thermal boundary conditions}\}. \quad (1)$$

The unknown functional structure Ψ is to be established through this parametric study based on the Nu data generated.

The heat transfer tests are initially performed at stationary states with Re = 4000, 8000, 12 000, 14 000. The indicative HTE effects of the present wavy channel are examined using the stationary results. A series of rotating experiments are subsequently followed at the parametric conditions summarized in Table 1. The rotational tests are initially performed for collecting the leading wall measurements after which the trailing wall measurements are taken by reversing the direction of rotation. Each set of rotational measurements is produced at fixed Re and Ro by adjusting the rotational speed and the pressure inside the test channel. For each rotational test, the coolant's flow rate is adjusted to obtain the tested Re at the

Table 1
Parametric ranges of test conditions in terms of Re, Ro and Bu.

Dimensionless parameter			Range
Reynolds number [Re]			4000–14 000
Rotation number [Ro]			0–0.22
Buoyancy number [$Bu = \beta(T_w - T_b)Ro^2(R/d)$]			0.003–0.11
Density ratio [$\beta(T_w - T_b)$]			0.03–0.09
Ro	*Re*	*Ro*	*Re*
Tested *Ro* for each *Re*			
0.2, 0.17, 0.12, 0.1, 0.08, 0.06, 0.04, 0.02	4000	0.08, 0.06, 0.04, 0.02	4000, 8000, 12 000
0.1, 0.08, 0.06, 0.04, 0.02	4000, 8000	0.06, 0.04, 0.02	4000, 8000, 12 000, 14 000

corresponding pressure. The required rotational speed for each tested *Ro* is accordingly determined and maintained. Both *Re* and *Ro* at the flow entrance can therefore be individually controlled. By varying the heater power to different levels at each set of *Re* and *Ro*, the density ratio and *Bu* are accordingly changed. However, the density ratio and *Bu* are the post-determined parameters. Following these procedures, *Re*, *Ro* and *Bu* can be adjusted independently.

At each *Re*–*Ro* combination tested, four ascending heater powers that raise the highest T_w levels to 333, 353, 373, and 403 K are supplied to create four different flow conditions with ascending buoyancy levels at the fixed *Re* and *Ro*. The isolated *Bu* effect on heat transfer is determined by comparing these *Nu* scans collected at different rotating buoyancy levels with fixed *Re* and *Ro*. All the T_w measurements are collected at the steady states which are assumed when the temporal wall temperature variations for the monitoring spots on the heating surface are less than ± 0.3 K after several successive scans with each time interval about 1 min.

The development of physically consistent *Nu* correlations requires assessing the individual Coriolis effects without buoyancy interactions. In this respect, it is not practical for heat transfer tests to acquire the *Nu* data at the zero-buoyancy condition due to the required wall-to-fluid temperature differences for *Nu* evaluations. Certain degrees of rotating buoyancy effects always coupled with *Ro* effects to influence the detected *Nu* from any heat transfer experiment. Alternatively, the separation of *Ro* effects from *Bu* interactions is performed by extrapolating the rotational *Nu* data into the limiting condition of $Bu = 0$ while *Re* and *Ro* remain at the tested values. This regression routine enables the identification of *Nu* levels at the zero-buoyancy conditions for all the sets of *Re* and *Ro* tested, which will be later demonstrated when the zero-buoyancy *Nu* values are determined. Along with the procedures devised to develop *Nu* correlations, the heat transfer physics indicative of the individual and interdependent *Re*, *Ro* and *Bu* influences over the leading and trailing walls of the rotating wavy channel are simultaneously resolved.

3.2. Data reduction

The local *Nu* over the wavy wall is experimentally defined using the equation of $Nu = q_f d/\{k_f(T_w - T_b)\}$ in which the local convective heat flux (q_f) is calculated by subtracting the heat loss flux from the total heat flux supplied. The characteristic of the external heat loss is determined by a number of calibration runs at five different rotating speeds. For each individual heat loss calibration run, the flow passage is blocked and filled with the thermal insulating fiberglass. When the heat loss test reaches the steady state, the heat flux supplied into the heating foils is balanced with the heat loss to the surrounding atmosphere. Heat loss fluxes and their corresponding averaged wall-to-ambient temperature differences ($T_w - T_\infty$) are accordingly correlated to determine the proportionality between the heat loss flux and the $T_w - T_\infty$ at each rotational speed tested. Such proportionality is treated as the heat loss coefficient which increases as the rotational speed increases. The regressive-type function that correlates the heat loss coefficient by the rotational speed is derived and built in to the data processing program to evaluate the heat loss flux on the local basis. As the T_w distributions over the wavy wall at each tested flow condition are not uniformly distributed, the distributions of $T_w - T_\infty$, the heat loss flux and therefore the q_f distributions over the wavy wall are not perfectly uniform. A review of the entire q_f data indicates the maximum non-uniformity of about 8.9% in q_f distributions.

The calculations of T_b variations inside the test channel are based on the principal of energy conversation. Having determined the streamwise q_f distribution along the test channel, the increase of T_b between two successive streamwise intervals is evaluated. This calculating procedure starts from the measured fluid entry temperature and ends at the flow exit. With each *Re* and *Ro* combination tested, the difference between the calculated and measured T_b at the exit of flow is less than ±10%, otherwise the data batch is disregarded and the heat transfer test is re-performed. With the T_b information, the local fluid properties such as the thermal conductivity of coolant are calculated. The subsequent parametric analysis is performed using the area-averaged *Nu* over the developed flow region ($_{byFD}$) of the wavy channel with the aim to devise the empirical $\overline{Nu}_{FD}$ correlations. The area used to define $\overline{Nu}_{FD}$ is the projected area from the point of fully developed flow.

The uncertainty analysis follows the method of estimating experimental uncertainties recommended by the editorial board of ASME J. Heat Transfer [33]. Most of the experimental uncertainties for the dimensionless parameters shown in equation (1) are attributed from the temperature measurements as the fluid properties in these parameters are temperature dependent. In respect of T_w measurements, our previous repeatability calibration tests for the present infra-red thermal image system have indicated the maximum uncertainty of ±0.7 K [34]. In general, the experimental uncertainties for *Nu* are reduced for the test results acquired from the high heater powers and *Re*. With the values of $T_w - T_b$ in the range of 28–56 K, the estimated maximum uncertainties for *Nu*, *Re*, *Ro* and *Bu* are about 9.2%, 5%, 4.2% and 9.1% respectively.

4. Results and discussion

4.1. Stationary results

With stationary results, the Nu_0 distributions reveal the heat transfer characteristics for the wavy channel and its HTE impacts in association with the flow structures generated within. Fig. 2 depicts the Nu_0 distributions over the skewed wavy wall for the present furrowed channel at $Re = 4000, 8000, 12\,000, 14\,000$. The characteristic pattern of Nu_0 distribution shared by all the results features the pitch-wise and wave-wise variations. The pitch-wise Nu_0 variations appear to be periodical with the peak (valley) values at the convergent–divergent throat (divergent–convergent bulge). Such pitch-wise Nu_0 variation is indicative of the accelerated flow with separations in each throat and the recirculating flow cells in the bulges, which are induced by the local pressure gradients and the separated shear layers tripped after the throats. The high (low) Nu_0 bands follow the skewness of wall-waves along the throats (bulges) with the 45° inclination to the bulk flow. This periodical pitch-wise Nu_0 distribution emerges from the streamwise heat transfer variation which shows the downstream Nu_0 elevation with the tendency to reach the developed level. Similar to pin-fin channels, the overall streamwise increase in Nu_0 reflects the nature of the flow development in this furrowed channel with their HTE effects gradually emerged toward the so-called periodically developed region where the pitch-wise Nu_0 distributions oscillate about a spatially mean Nu_0. In this regard, the number of wall-waves required to reach the developed flow region where the full HTE effects emerge tends to be decreased as *Re* increases. Such upstream movement of the frontier with full HTE effects is seen in Fig. 2 by cross examining the Nu_0 plots obtained with different *Re*. It is worth noting that, although the pitch-wise Nu_0 profile indicates the spatially low heat transfer rates in the bulges, heat transfer augmentations from the Dittus–Boelter correlation values (Nu_∞) are still evident over the entire wavy wall. The *Re* range of 4000–14000 for this particular furrowed channel enables the macroscopic wall-to-core mixing by the roller vortices in the free shear layer that trigger small oscillations in core flows [29] and promotes the turbulent activity, which causes the shrinkage of the

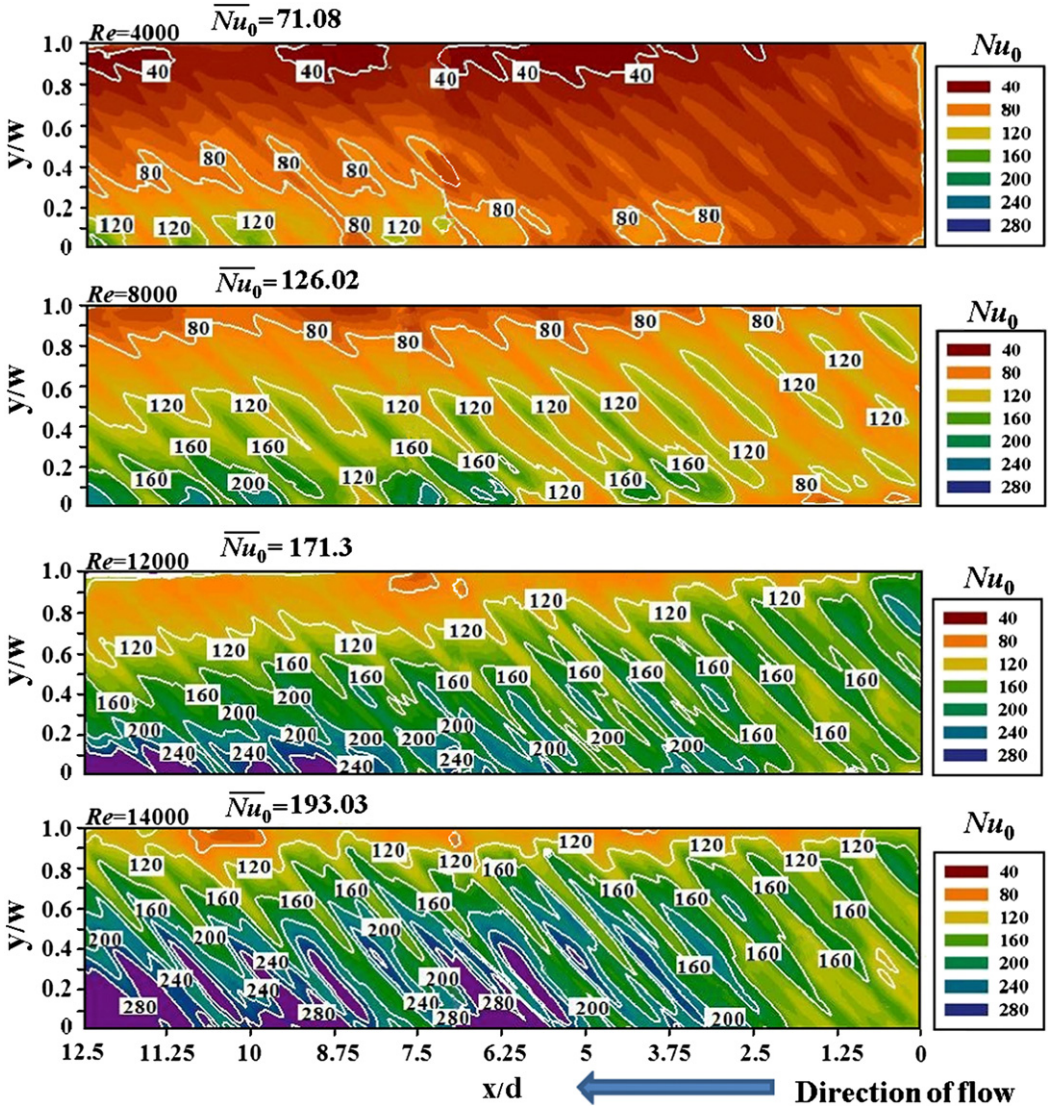

Fig. 2. Nu_0 distributions over skewed wavy wall in furrowed channel at Re = 4000, 8000, 12 000, 14 000.

separation bubble in each bulge [32]. These fluid mechanisms [29,35] are also responsible for the upstream expansion of the developed flow region with full HTE impacts showed in Fig. 2 as Re increases. As a result, the increase of the area-averaged Nu_0 over the entire wavy wall ($\overline{Nu}_0$) when Re is increased, as indicated on each plot of Fig. 2, is partially attributed to the upstream expansion of the developed flow region. With turbine blade cooling applications, the developed flow region occupies the most of an internal coolant channel due to the large length to hydraulic-diameter ratio of the channel. Therefore the parametric analysis developed here focuses on the area-averaged results for the developed flow region in order to improve the generality of the heat transfer correlation derived by this study.

Another point worth noting which differentiates the heat transfer characteristics for the present test channel from those over the traditional wavy channels with transverse wall-waves [27–29,35] is the wave-wise Nu_0 variations tripped by these skewed wall-waves. In this respect, the local Nu_0 values consistently decay along each skewed wall-wave from the side edge of $y/W = 0$ toward another side edge of $y/W = 1$. Similar to the channel roughened by the angled ribs, the wave-wise Nu_0 variation indicates that these skewed wall-waves can induce the cross-sectional secondary flows. Therefore the Nu_0 distributions displayed in Fig. 2 show the combined effects of the streamwise wall-to-core macroscopic mixings and the strong cross-sectional secondary flows induced by the inclined wall-waves. With the strong sectional secondary flows induced by the skewed wall-waves in the present furrowed channel, the recirculating flow cells in bulges for the likewise furrowed channel with transverse wavy walls are "disturbed" and the separations, shear layers as well as the turbulence activities over the transverse wavy walls [27–29,35] are altered. Due to the sectional secondary flows in the furrowed channel with skewed wall-waves, further HTE effects from the likewise channel with transverse wavy walls were reported in our previous work [30].

As the developed flow region is readily identified from Fig. 2 at each tested Re, the area-averaged Nu_0 over the developed flow region ($\overline{Nu}_{0FD}$) are determined. The variation of $\overline{Nu}_{0FD}$ against Re is depicted in Fig. 3. In addition, the normalized $\overline{Nu}_{0FD}/Nu_\infty$ ratios as well as the $\overline{Nu}_0$ data obtained by averaging the local Nu_0 values over the ***entire*** wavy wall are included in Fig. 3. As compared in Fig. 3, $\overline{Nu}_{0FD}$ is constantly higher than $\overline{Nu}_0$ over the Re range of 4000–14000; but the difference between $\overline{Nu}_{0FD}$ and $\overline{Nu}_0$ is systematically reduced as Re increases. Such reduced $\overline{Nu}_{0FD}$-to-$\overline{Nu}_0$

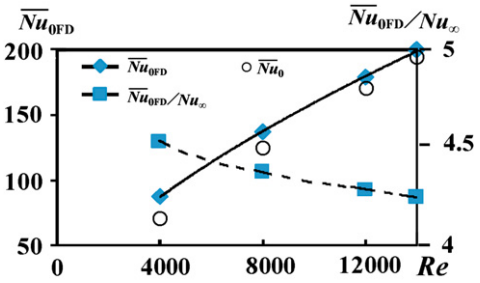

Fig. 3. Variations of $\overline{Nu}_{0FD}$, $\overline{Nu}_0$ and $\overline{Nu}_{0FD}/Nu_\infty$ against *Re*.

difference at the higher *Re* is attributed to the *Re*-driven upstream expansion of the developed flow region revealed by Fig. 2. As *Re* increases, $\overline{Nu}_{0FD}$ and $\overline{Nu}_{0FD}/Nu_\infty$ respectively increases and decreases. The ratios of $\overline{Nu}_{0FD}/Nu_\infty$ and $\overline{Nu}_0/Nu_\infty$ respectively fall between 4.57–4.23 and 4.23–4.08 with $4000 \le Re \le 14\,000$. Using the area-averaged heat transfer data collected in Fig. 3, $\overline{Nu}_{0FD}$ and $\overline{Nu}_0$ are correlated by *Re* using the power-law function so that the limiting condition of diminished forced convective capability ($\overline{Nu}_{0FD} \to 0$) as $Re \to 0$ is automatically satisfied. The $\overline{Nu}_{0FD}$ and $\overline{Nu}_0$ correlations for the present test channel are respectively derived as equations (2) and (3).

$$\overline{Nu}_{0FD} = 0.176\, Re^{0.738} \tag{2}$$

$$\overline{Nu}_0 = 0.125\, Re^{0.77} \tag{3}$$

The maximum discrepancies between the calculated values of $\overline{Nu}_{0FD}$ and $\overline{Nu}_0$ using equations (2) and (3) and the experimental measurements are respectively less than ±20% and ±15%. As the *Re* exponents in equations (2) and (3) are both less than the *Re* exponent of 0.8 in Dittus–Boelter correlation, the ratios of $\overline{Nu}_{0FD}/Nu_\infty$ and $\overline{Nu}_0/Nu_\infty$ is decreased as *Re* increases as seen in Fig. 3.

4.2. Rotational results

In the wavy channel, the separated flows tripped by the undulant walls along with the complex flow instabilities triggered at the shear layers between the core-stream and the flow cells entrapped in the bulges have promoted the macroscopic core-to-wall mixings with the attendant HTE effects in the stationary channel [27–29,35]. The design of a wavy channel for turbine rotor blade cooling must take into consideration the Coriolis and rotating buoyancy effects which modify the flow structures from the corresponding stationary scenarios. In the present test channel with the cross-sectional aspect ratio of 4, the side-wall effect is likely to be confined to the region close to it, and the core region of the rotating channel may not be featured by a typical pair of Coriolis vortices but a flow structures with multiple vortices initiated by the undulant perimeter of the wavy channel. To date, the information for such an assessment for flow structure has not been available. However, the full *Nu* scans over the rotating wavy wall offer the direct assessments of the rotational effects on heat transfer through the comparative study with the stationary results. Fig. 4 compares the *Nu* scans observed over the rotational leading (stable) and trailing (unstable) wavy walls with the stationary counterparts for *Ro* = (*a*) 0.1 and (b) 0.22 at *Re* = 4000 with the area-averaged Nusselt numbers over the entire wavy wall ($\overline{Nu}$) indicated. The buoyancy parameters in terms of $\beta(T_w - T_b)$ for the comparative groups in Fig. 4 is selected as 0.01 at *Ro* = 0.1 and 0.04 at *Ro* = 0.22 in order to keep the rotating buoyancy level fixed for each set of the three plots collected in Fig. 4-a or b. As typified by Fig. 4, due to the Coriolis effects, the trailing wall constantly operates at the higher *Nu* ($\overline{Nu}$) levels than the leading and stationary counterparts for all the *Ro* examined. On the leading wall, the local *Nu* and $\overline{Nu}$ are both decreased from the stationary datum at *Ro* = 0.1 as depicted in Fig. 4-a; but the increase of $\overline{Nu}$ accompanying by the regionally local *Nu* elevations from the stationary results are seen in Fig. 4-b at *Ro* = 0.22. Clearly, the heat transfer modification on the rotational leading and trailing walls from the stationary conditions are location dependent. As shown in Fig. 4-a, the local *Nu* elevations (reductions) from the stationary references on the trailing (leading) wall tend to be initiated from the developed flow region along the side edge with obtuse wave-angles (obtuse edge) where the higher wave-wise Nu_0 values are developed. Further increasing *Ro* from 0.1 to 0.22, the variations of *Nu* distribution as seen from Fig. 4-a to b reveal such location dependent Coriolis effects on both trailing and leading walls. In this respect, the region with considerable heat transfer elevations from the stationary references on the trailing wall expands along the wave-wise direction from the obtuse edge to the side edge with acute wave-angles (acute edge) as well as toward the upstream region in the streamwise direction. However, as *Ro* increases from 0.1 to 0.22, the leading wall $\overline{Nu}$ level is initially reduced from $\overline{Nu}_0$ at *Ro* = 0.1 and followed by the subsequent elevation from $\overline{Nu}_0$ at *Ro* = 0.22. The region where shows such evident *Ro*-driven impeding-to-improving heat transfer variation on the leading wall also develops along the obtuse edge in the developed flow region. But while the local heat transfer improvements are emerging over the developed flow region on the leading wall at *Ro* = 0.22 as seen in Fig. 4-b, the heat transfer impediments from the stationary references still remain evident in its developing flow region. Further $\overline{Nu}$ elevations on the leading wall driven by increasing *Ro* from 0.22 onward are expected to follow the expanding manner of the heat transfer improvement region in both streamwise and wave-wise directions over the trailing wall. The manner of *Nu* variations over the leading and trailing walls responding to the increase of *Ro* from 0 to 0.22 displayed by Fig. 4 reveals that the most evident Coriolis effects are initiated at the developed flow region from which the Coriolis impacts are expanded to cover the entire rotational leading and trailing walls as *Ro* increases.

With the present infra-red thermography, the most unique advantage to the generation of heat transfer data with cooling applications to gas turbine rotor blade is its accessibility to examine the detailed rotating buoyancy effects on *Nu* distributions over the entire rotating surface, which has not been available to date. Fig. 5 displays the *Nu* scans detected from the rotational leading and trailing walls with three ascending buoyancy levels at *Re* = 8000 and *Ro* = 0.1. For each *Nu* scan detected in Fig. 5, the characteristic Coriolis effects on heat transfer distributions over the leading or trailing wall follow the typical results revealed by Fig. 4 but with the attendant heat transfer reductions over both leading and trailing wavy walls as the buoyancy level systematically increased. Unlike the spatial heat transfer modifications responding to the increase of *Ro* as shown in Fig. 4, the spatial *Nu* variations responding to the increase of buoyancy level over the leading and trailing walls as seen in Fig. 5 are amplified from the developed flow region along the **acute** edge where the lower *Nu* values over each skewed wall-wave are developed. Driven by the increased buoyancy level at the selected *Ro* as seen from Fig. 5-a → b → c for leading wall and from Fig. 5-d → e → f for trailing wall, the low heat transfer regions with the hotter surfaces in the developed flow region expand in the upstream direction as well as in the wave-wise direction from the **acute**-to-**obtuse** edges with the attendant local *Nu* reductions. It is also interesting to note in Fig. 5 that the *Nu* values near the inlet differ depending on *Bu* for the same *Re* and *Ro*. This particular data trend is followed by all the rotational results

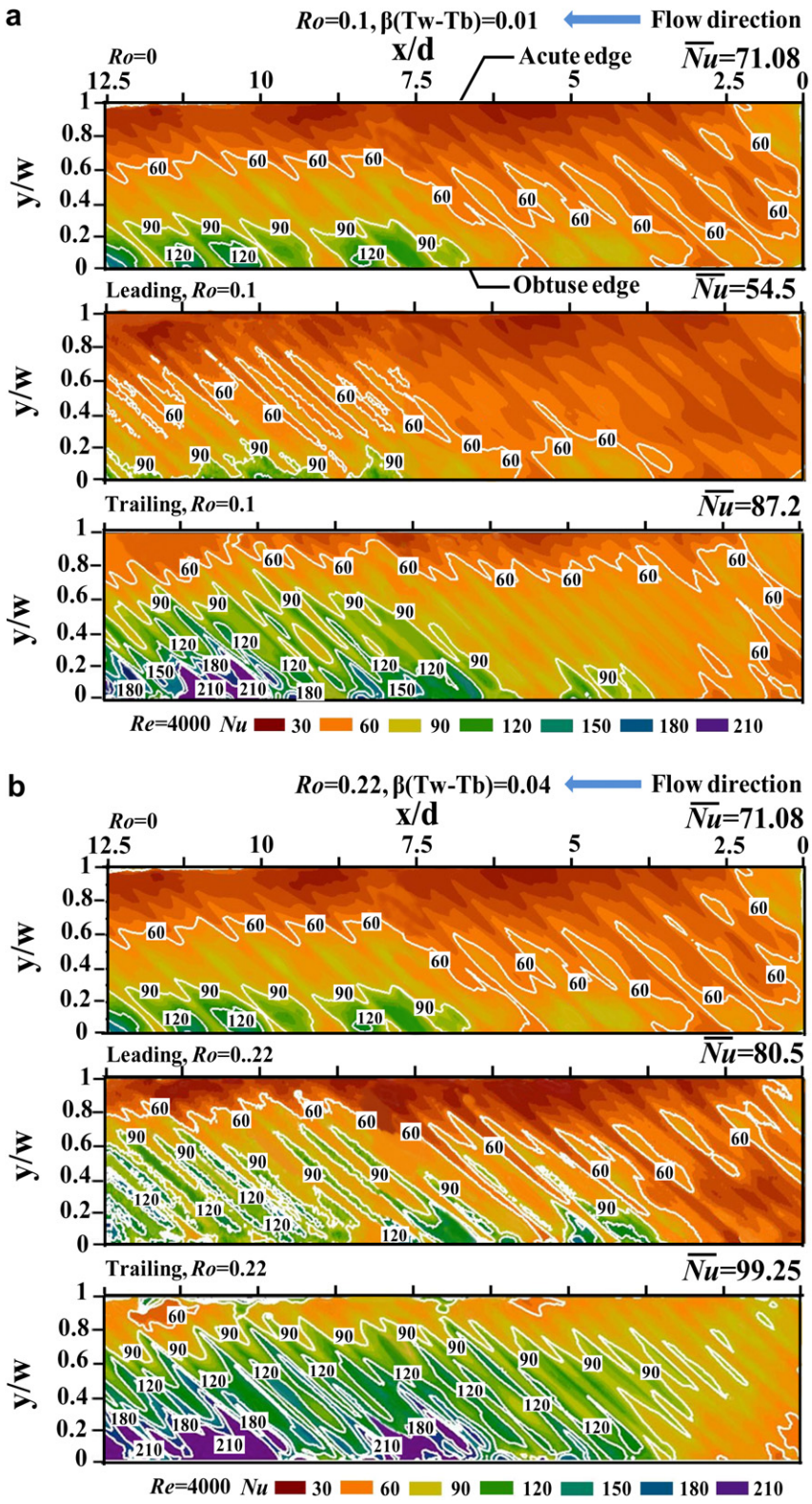

Fig. 4. Comparison of Nusselt number distributions over rotational leading and trailing walls with stationary results with $Re = 4000$ at (a) $Ro = 0.1$, (b) $Ro = 0.22$.

obtained from this investigation. For a square channel with 45° ribs [3], the increase of *Bu* has caused the initial reduction in *Nu* over the leading (stable) wall. However for the trailing (stable) wall, *Nu* increases consistently as *Bu* increases. The present *Bu* effect for this rotating geometry is different from the previous results using the square channel with surface ribs [3]. As the rotating radius of the flow entry plane from the center of the shaft is about 10 d, the centrifugal acceleration prevails over the entire pressurized rotating test section. At the steady-state condition, this set of results typified by Fig. 5 indicates that the rotating buoyancy effect prevails over the entire rotating channel with its degree of impact depending on the developing and developed flow regions.

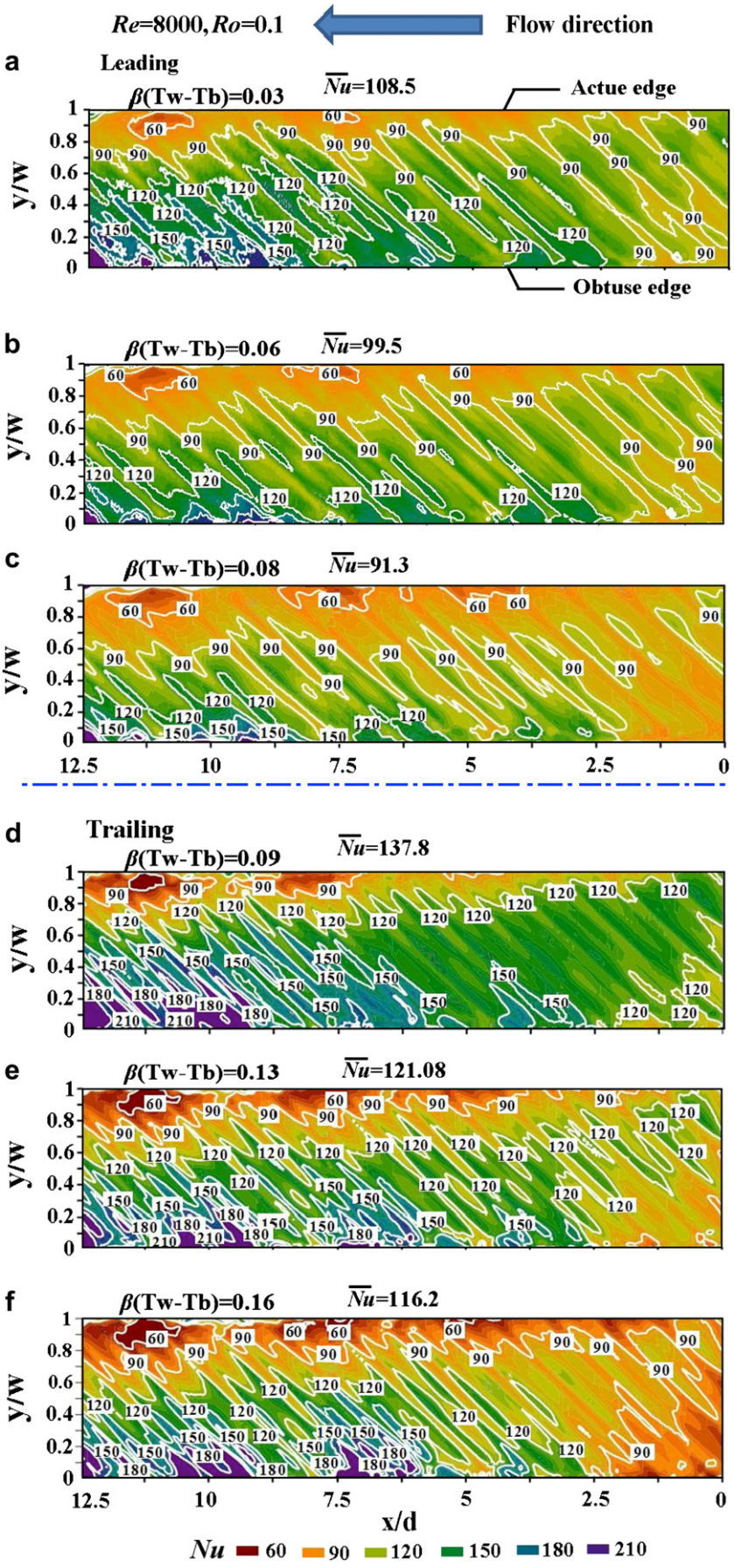

Fig. 5. Rotating buoyancy effect on *Nu* distributions over leading and trailing walls at $Re = 8000$, $Ro = 0.1$.

The reduced local *Nu* coupled with the streamwise and wave-wise expansions of the low heat transfer region have led $\overline{Nu}$ over the leading and trailing walls to systematic reductions from the "zero-buoyancy" datum. With the parametric conditions examined here, the overall reduction in local *Nu* over both the rotational leading and trailing walls is likely to reflect the suppressed turbulent activities while the expansion of the low *Nu* region from the acute edge is indicative of the modification in flow structures due to the increase of buoyancy level at the selected *Ro*. As the increase of *Ro* from 0 to 0.04 incurs an initial shrinkage of the high *Nu* region on the leading wall from the stationary conditions, the acute-to-obtuse expansion of the low *Nu* region driven by the enhanced buoyancy effect can worsen the heat transfer impediments over the leading wall at low *Ro* conditions. But on the trailing wall, the increase of *Ro* always leads to the obtuse-to-acute expansion of the high *Nu* region without experiencing the *Ro*-driven impeding heat transfer effect. As a result, the combined *Ro* and *Bu* effects on heat transfer develop differently on the leading and trailing walls due to the different *Ro*-driven wave-wise expansions for the high (low) *Nu* regions along the obtuse (acute) edge at $Ro \leq 0.04$. Therefore the coupling *Ro*−*Bu* impact on *Nu*, which is referred to as the φ_2 function in the later parametric analysis section, can be correlated by *Ro* as demonstrated there.

Figs. 6 and 7 respectively compare the *X*-wise and *Y*-wise *Nu* variations at the selected buoyancy levels along the centerline of (a) leading (b) trailing walls for $Ro = 0, 0.06, 0.1, 0.22$ at $Re = 4000$. The characteristic pattern of stationary X-wise Nu_0 profile is followed by all the *Ro* results collected in Fig. 6 with local *Nu* peaks (valleys) emerging at the throats (bulges) over the leading and trailing wavy walls. Even with the presence of Coriolis and rotating buoyancy effects, the typical throat-to-bulge *Nu* variations due to the core-to-wall mixing triggered by the undulating walls still persist in the rotating channel. While the increase of *Ro* keeps elevating the *Nu* levels along the trailing centerline, the local *Nu* along the leading centerline is reduced from the stationary ($Ro = 0$) reference at $Ro = 0.06$, recovered at $Ro = 0.1$ and improved at $Ro = 0.22$. The larger *Nu* spans driven by varying *Ro* from 0 to 0.22, which indicate the larger degrees of Coriolis effects are consistently seen in the developed flow region of Figs. 6-a and b. Fig. 7 compares the *Y*-wise *Nu* variations in the developed flow region at $x/d = 9.71$ having the flow conditions identical with those in Fig. 6. As the spanwise section at $x/d = 9.71$ for the present wavy channel traverses five throats, five local *Nu* peaks at the centers of these throats, which present the striking contract to the *Nu* valleys at the centers of bulges, are observed in Fig. 7. Nevertheless, the streamwise *Nu* oscillations with the sharp fall after the center of each throat as seen in Fig. 6 are not observed in the *Y*-wise *Nu* oscillations at the locations aside each center of throat in Fig. 7. With the present *Ro* range ($Ro \leq 0.22$), the entrapments of flow cells in the bulges are still dominant by the streamwise bulk flow rather than the typical Coriolis secondary flows in the square-sectioned channel. As a result, the patterns of *Nu* oscillations over a wave pitch in the streamwise and spanwise directions are different as compared by Figs. 6 and 7. But with the presence of Coriolis forces in the

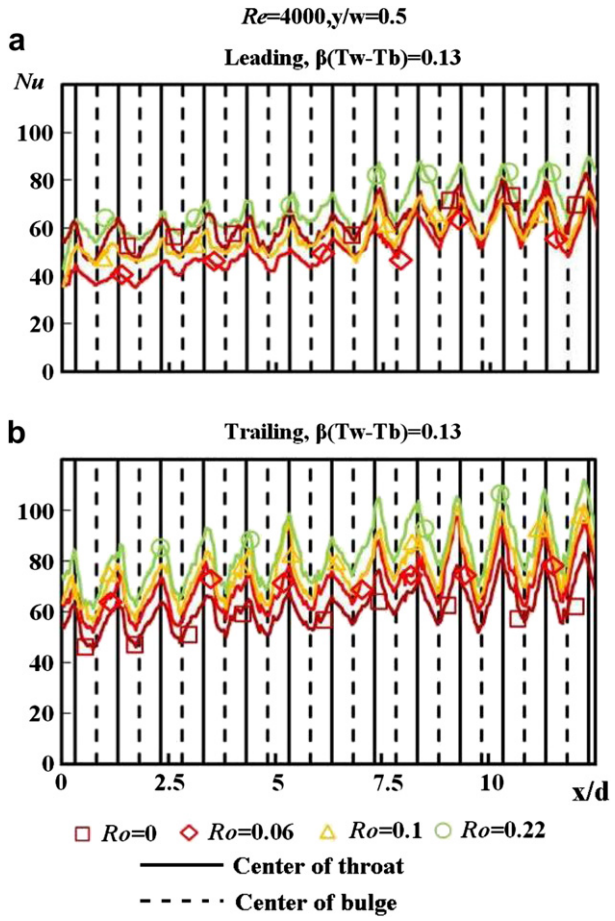

Fig. 6. *X*-wise Nusselt number profiles along (a) leading, (b) trailing centerline with $Re = 4000$ at $Ro = 0, 0.06, 0.1, 0.22$.

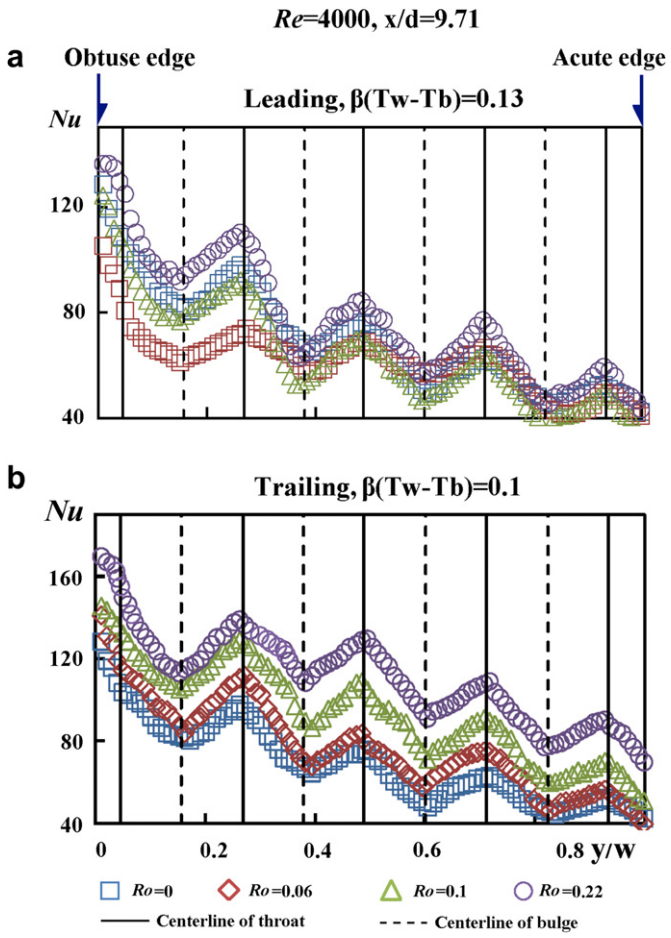

Fig. 7. *Y*-wise Nusselt number profiles at $x/d = 9.71$ on (a) leading, (b) trailing walls with $Re = 4000$ at $Ro = 0, 0.06, 0.1, 0.22$.

direction toward the trailing wavy wall, the obtuse-to-acute secondary flows tripped by the skewed wall-waves are closely affected. The vortical interactions between the wall-wave induced secondary flows and the flow complexities induced by Coriolis forces, which are *Ro* dependent, put forth the variable skewness in the *Y*-wise *Nu* variations over the leading and trailing walls as noticed in Fig. 7.

In the regard of *Ro* dependency on the *Y*-wise *Nu* skewness, the leading *Y*-wise *Nu* profile at $Ro = 0.06$ is considerably flattened from its stationary and rotating counterparts collected in Fig. 7-a. Such *Ro* dependent differences in the *Y*-wise *Nu* skewness reflect the different Coriolis effects along the obtuse and acute edges on the rotating wavy wall. Justified by the large (small) *Nu* spans at the leading obtuse (acute) edge as *Ro* increases from 0 to 0.22 as seen in Fig. 7-a, the Coriolis effects on the heat transfer performances over the rotational leading wall are more pronounced at the obtuse edge than its acute edge. When the Coriolis effects reduce the heat transfer rates on the leading wall at $Ro = 0.06$, the more pronounced obtuse-edge *Nu* suppressions relative to its acute counterpart moderate the stationary obtuse-to-acute Nu_0 skewness. When the Coriolis effects improve leading wall heat transfer at $Ro = 0.22$, the more *Nu* elevation at the obtuse edge than its acute counterpart on the rotational leading wall enhances the *Y*-wise *Nu* skewness from the stationary condition. Therefore the overall *Y*-wise *Nu* skewness at $Ro = 0.06$ and 0.22 are respectively moderated and enhanced from the stationary reference ($Ro = 0$) as seen in Fig. 7-a. On the trailing wall, the acute-edge *Nu* spreads driven by increasing *Ro* from 0 to 0.22 are considerably larger than those at the acute edge on the leading wall. Because the Coriolis effects consistently elevate the local *Nu* over the rotational trailing wall, the *Ro* dependent variations in the *Y*-wise *Nu* skewness over the trailing wall, as seen in Fig. 7-b, are not as prominent as those developed over the leading wall. Nevertheless, in view of the relative heat transfer impediments or improvements from the stationary references, the variations of *Y*-wise *Nu* responding to the increase of *Ro* from 0 to 0.22 follow the results depicted by Fig. 6.

The *Nu* variations responding to four ascending buoyancy levels along the streamwise centerline and in the spanwise direction at $x/d = 9.71$ in the developed flow region with $Ro = 0.1$, $Re = 8000$ are respectively depicted by Figs. 8 and 9. At $Ro = 0.1$, local *Nu* over the leading and trailing walls decrease consistently as the buoyancy level increases. In particular, although the Coriolis effects elevate local *Nu* on the trailing wall, the increase of $\beta(T_w - T_b)$ from 0.03 to 0.16 systematically reduces the local *Nu* toward the stationary level as seen in Figs. 8-b and 9-b. If such buoyancy driven data trend on trailing wall is followed onward at the higher buoyancy levels of $\beta(T_w - T_b) > 0.16$, the favorable Coriolis effects on heat transfer over the trailing wall can be offset. Nevertheless, the rotating buoyancy effects appear to be *Ro* dependent which will be illustrated in the later parametric analysis. The considerable *Nu* reductions driven by increasing $\beta(T_w - T_b)$, which has disparity in the *Nu* spreads driven by varying *Ro* in Fig. 7-a, is observed at the acute edge of leading wall showed by Fig. 9-a. Due to the consistently impeding buoyancy effect over the leading and trailing walls, the overall *Y*-wise *Nu* skewness on the leading and trailing walls are not significantly altered from the stationary profile as seen in Fig. 9. As the rotating buoyancy effects typified by Figs. 8 and 9 are followed by all the rotating test results, the rotating buoyancy effects prevail over the entire rotational leading and trailing walls but with the lesser spatial dependency from the condition for the Coriolis effects.

4.3. Parametric analysis and heat transfer correlation

The parametric analysis developed by this research group [9–12,24–26] for analyzing the heat transfer performance of

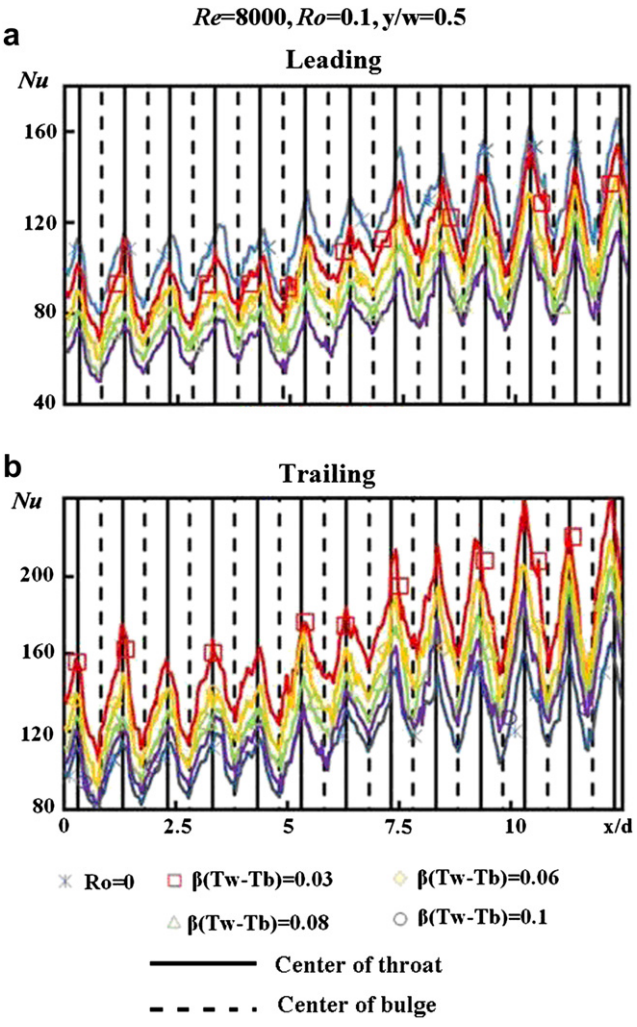

Fig. 8. *X*-wise Nusselt number profiles along (a) leading, (b) trailing centerline with four different rotating buoyancy levels at $Re = 8000$ and $Ro = 0.1$.

rotating channels has been focused on the local basis using the heat transfer data derived from the thermocouple measurements. Having acquired the full *Nu* scans over the rotational wavy walls, the area-averaged Nusselt number over the developed flow region ($\overline{Nu}_{FD}$) at each test condition is obtained. Variations of $\overline{Nu}_{FD}$ from the non-rotating references ($\overline{Nu}_{0FD}$) are parametrically analyzed in this section with the attempts to derive the physically consistent $\overline{Nu}_{0FD}$ correlation as well as to disclose the isolated and interdependent *Re*, *Bu* and *Ro* impacts on $\overline{Nu}_{0FD}$. Due to the lack of full *Nu* scan that can reflect the rotating buoyancy effects over rotating surfaces, the previous attempt to isolate the *Re* impacts from the manifesting rotational effects was performed on the local basis by way of presenting the local heat transfer measurement in terms of Nu/Nu_0. It has been shown that the consistent success to converge the local Nu/Nu_0 data generated with different *Re* but at the same *Ro* and *Bu*, which therefore verifies the isolation of *Re* impacts from the combined *Ro* and *Bu* effects by way of analyzing the heat transfer data in terms of Nu/Nu_0 [9–12,24–26]. This attempt is now testified using the various *Nu* scans collected from the leading and trailing walls with different *Re* but at the same *Ro* and *Bu* for the present rotating wavy channel. The spatial variations of Nu/Nu_0 over the rotational leading and trailing walls at $Ro = 0.06$ with different $Re = 4000$, 8000, 12 000 and 14 000 are compared in Fig. 10-a and b respectively. The buoyancy parameters for each

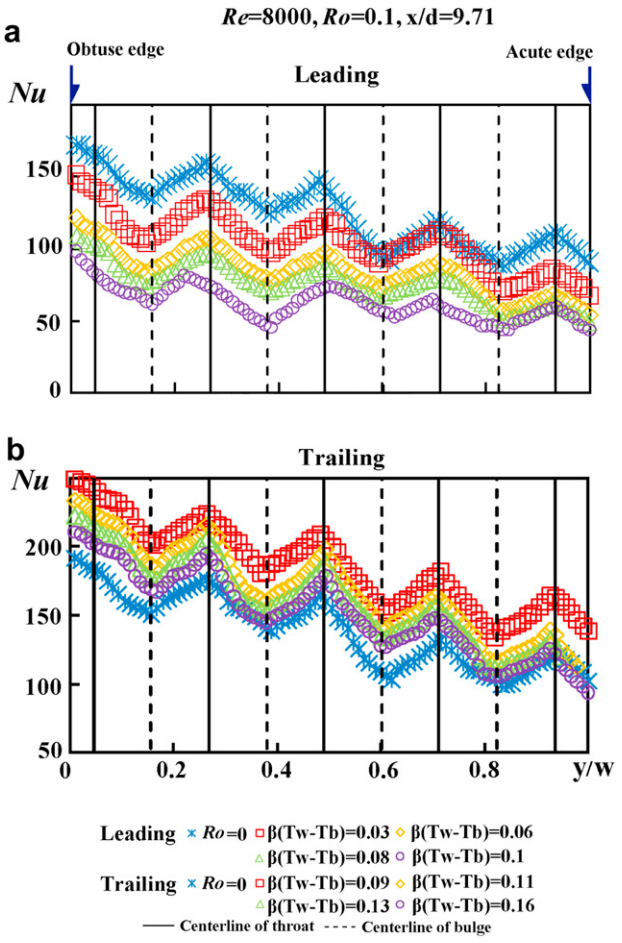

Fig. 9. *Y*-wise Nusselt number profiles at $x/d = 9.71$ on (a) leading, (b) trailing walls with four different rotating buoyancy levels at $Re = 8000$ and $Ro = 0.1$.

comparative group are selected at the similar nominal values with variances less than 10%. As seen in Fig. 10, the distributions of Nu/Nu_0 obtained with four different Re ranging from 4000 to 14 000 over the leading and trailing walls reveal the general trend with the higher Nu/Nu_0 at the throats in contrast to the lower Nu/Nu_0 at the bulges. Clearly, the influences of rotation on heat transfer performances are spatial functions. However, in the developing flow region, the values as well as the distributing patterns of Nu/Nu_0 over both leading and trailing walls vary with Re. This demonstrates that the Re impacts on Nu over the developing flow region are coupled with the Ro and Bu effects. In other words, the developments of Coriolis and buoyancy influences on heat transfer are affected by the inertial forces for the present rotating channel. Further downstream the developing flow region, the distributions of Nu/Nu_0 for each comparative group over the leading and trailing walls as shown in Fig. 10 (a)(b) follow the same pattern with the similar values in the developed flow region. Therefore the isolation of Re impact form the rotational Ro–Bu influences on Nu over the developed flow region is permissive by way of presenting the heat transfer levels in terms of Nu/Nu_0. Therefore, the convergence of the various area-averaged Nu/Nu_0 over the developed flow region obtained with different Re at the fixed Ro and Bu is expected. Fig. 11 compares the normalized $\overline{Nu}_{FD}/\overline{Nu}_{0FD}$ obtained from different Re but at the same Ro with the similar Bu. At $Ro = 0.02, 0.04, 0.06$ with $Re = 4000, 8000, 12\,000, 14\,000$ and $Ro = 0.08$ with $Re = 4000$ and 8000, the various $\overline{Nu}_{FD}/\overline{Nu}_{0FD}$ ratios obtained from different Re converge into the tight data bands for leading and trailing walls. This result demonstrates that the Re impact indexed as $Re^{0.738}$ in equation (2) can be used to isolate its effect from the rotational influences on $\overline{Nu}_{FD}$. Having isolated the Re impact by quantifying the rotational heat transfer performance in terms of $\overline{Nu}_{FD}/\overline{Nu}_{0FD}$, the synergetic Ro–Bu influence on the area-averaged heat transfer performances over the developed flow region are subsequently examined. Fig. 12 shows the variations of $\overline{Nu}_{FD}/\overline{Nu}_{0FD}$ against Bu at all the fixed Ro tested. As indicated by Fig. 12-a and b, each Ro controlled data series driven by the increase of Bu descends linearly. The magnitude of the slope for each Ro controlled data series as shown in Fig. 12-a and b systematically decreases as Ro increases. The isolated Bu effect impairs heat transfer with its impact on $\overline{Nu}_{FD}$ gradually weakened as Ro increases. It is clear that the Bu effect on $\overline{Nu}_{FD}$ is Ro dependent. The Ro–Bu interdependency becomes evident by plotting the various slopes collected from Fig. 12-a and b against their associated Ro and can be expressed as the Ro controlled function. Nevertheless, to reveal the Ro effect on $\overline{Nu}_{FD}$ in isolation from the direct heat transfer measurements is not practical as the finite wall-to-fluid temperature differences that can initiate Bu interactions are inevitable if Nu is experimentally defined. In the quest of a physically consistent $\overline{Nu}_{FD}$ correlation, it is meaningful to identify the so-called zero-buoyancy heat transfer data by extrapolating each Ro controlled data series in Fig. 12 to the limiting condition of $Bu = 0$ with diminished buoyancy level using the regressive-type analysis. This type of linear extrapolation routine based on each Ro controlled data series collected in Fig. 12 leads to the generation of $\overline{Nu}_{FD}/\overline{Nu}_{0FD}$ data at the zero $\beta(T_w - T_b)$ condition with $Bu = 0$. Fig. 12-a and b indicate these fitted lines with the extrapolated zero-buoyancy $\overline{Nu}_{FD}/\overline{Nu}_{0FD}$ values indicated on the vertical axis of each plot. Justified by the well curve-fits using the linear correlations as seen in Fig. 12, the $\overline{Nu}_{FD}/\overline{Nu}_{0FD}$ correlation is formulated as:

$$\overline{Nu}_{FD}/\overline{Nu}_{0FD}\varphi_1\{Ro\} + \varphi_2\{Ro\} \times Bu \tag{4}$$

In equation (4), φ_1 and φ_2 are functions of Ro which are respectively determined as the intercept and the slope of each linear fit collected in Fig. 12. The φ_1 value accounts for the $\overline{Nu}_{FD}/\overline{Nu}_{0FD}$ ratio at the zero-buoyancy condition. Variations of φ_1 against Ro depicted by Fig. 13-a reveal the sole Coriolis force effects on the area-averaged heat transfer performances over the developed flow region. As φ_2 quotes for the various slopes of the fitted lines collected in Fig. 12, the plot of φ_2 against Ro as seen in Fig. 13-b reveals the interdependency of the rotating buoyancy effect on Ro. As indicated by Fig. 13-b, the exponential decays of φ_2 magnitudes against Ro for leading and trailing walls feature the weakened Bu impacts on $\overline{Nu}_{FD}/\overline{Nu}_{0FD}$ as Ro increases. Acting by the Coriolis effects alone in this rotating wavy channel, the zero-buoyancy $\overline{Nu}_{FD}/\overline{Nu}_{0FD}$ ratios on the trailing wall increase consistently as Ro increases. The trailing $\overline{Nu}_{FD}/\overline{Nu}_{0FD}$ ratio at $Ro = 0.22$ reaches about 1.5 as shown in Fig. 13-a. But the isolated Ro effect initially reduces the leading $\overline{Nu}_{FD}/\overline{Nu}_{0FD}$ ratio from unity to the minimum value of 0.85 at $Ro = 0.04$. By way of increasing Ro from 0.04 onward, the leading $\overline{Nu}_{FD}/\overline{Nu}_{0FD}$ values are recovered and lead to the ratio about 1.1 at $Ro = 0.22$. With $0 \le Ro \le 0.22$, the leading and trailing φ_1 values displayed in Fig. 13-a can be both correlated by the complex exponential function. As the Bu impacts in the present Ro range undermine heat transfer performances on leading and trailing walls, the $\overline{Nu}_{FD}/\overline{Nu}_{0FD}$ values indicated in Fig. 13-a will be further reduced if the combine Ro–Bu influences are considered. Within the present experimental conditions with involvements of the impairing Bu effects on heat transfer, the ranges of $\overline{Nu}_{FD}/\overline{Nu}_{0FD}$ ratios on leading and trailing walls are 0.77–1.03 and 1.02–1.46 respectively. Converting the ranges of heat transfer modifications from the stationary datum in terms of $\overline{Nu}_{FD}/\overline{Nu}_{0FD}$ to the relative heat transfer enhancements over the Dittus–Boelter level in terms

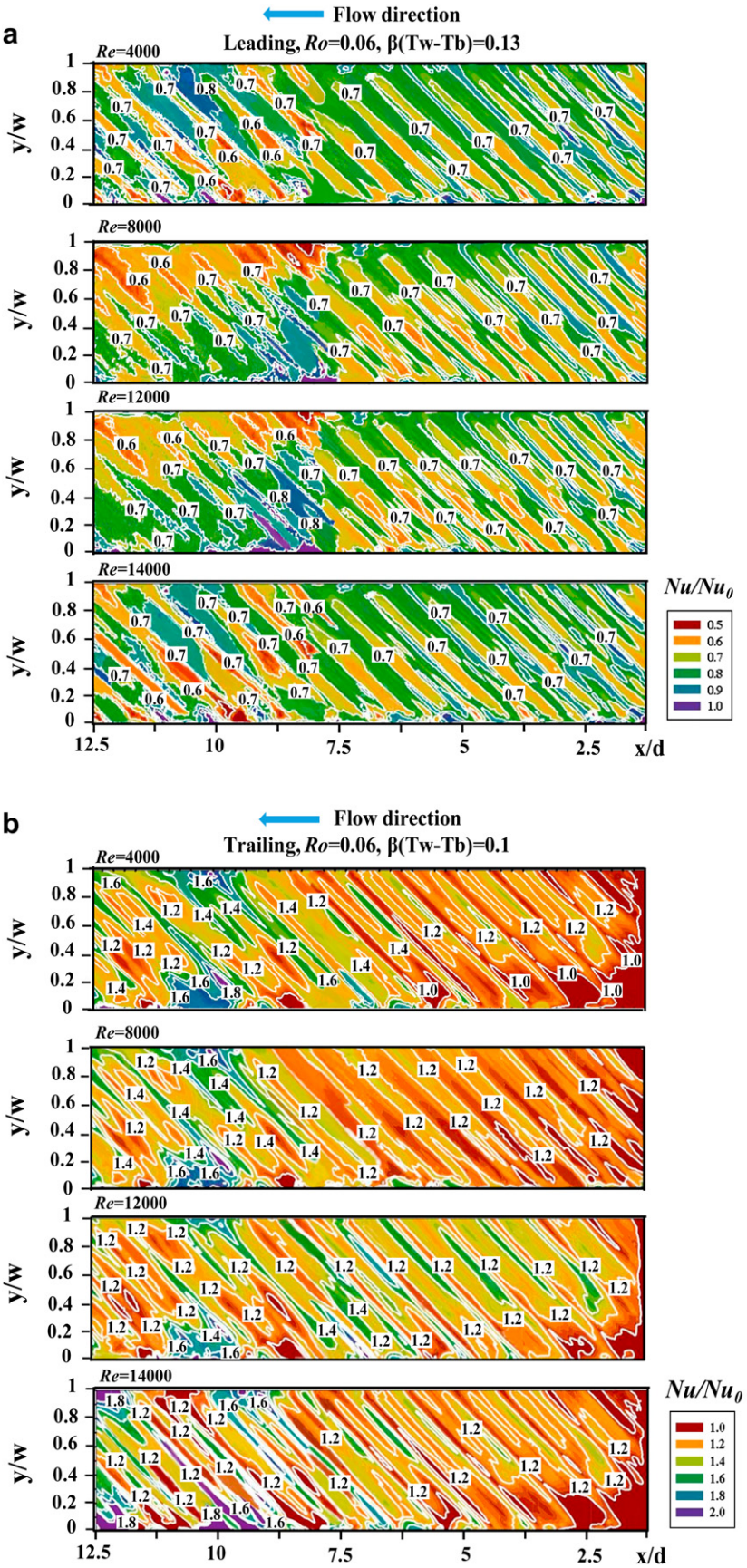

Fig. 10. Distributions of Nu/Nu_0 over (a) leading, (b) trailing wavy walls with Re = 4000, 8000, 12 000, 14 000 at fixed Ro = 0.06 and nominal buoyancy levels.

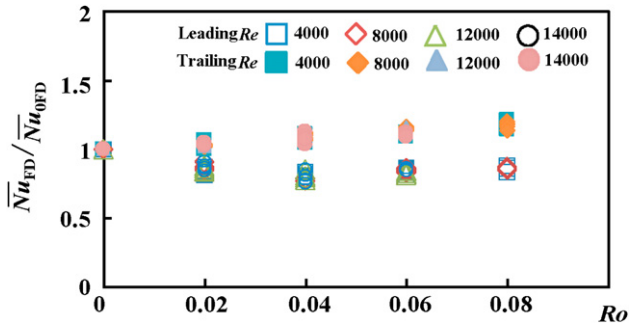

Fig. 11. Various $\overline{Nu}_{FD}/\overline{Nu}_{0FD}$ ratios obtained from different *Re* but at the same *Ro* with similar *Bu*.

of $\overline{Nu}_{FD}/Nu_{\infty}$ give the HTE impacts generated by the present rotating wavy walls; which fall in the ranges of 3.4–4.3 and 4.2–6.4 for the leading and trailing walls respectively. After correlating all the data trends depicted in Figs. 12 and 13, a set of $\overline{Nu}_{FD}$ correlations that evaluates for leading and trailing walls of the present rotating wavy channels is obtained as equations (5) and (6) respectively.

$$\overline{Nu}_{FD} = (0.176Re^{0.738}) \times \{(0.741 + 1.72 \times Ro + 0.259e^{-32.7 \times Ro}) + (-3.19 + 9.6 \times Ro - 347e^{-83.9 \times Ro}) \times Bu\} \text{ (Leading)} \quad (5)$$

$$\overline{Nu}_{FD} = (0.176Re^{0.738}) \times \{(1.36 + 0.669 \times Ro - 0.36e^{-12.6 \times Ro}) + (-4 + 11.4 \times Ro - 415e^{-52.5 \times Ro}) \times Bu\} \text{ (Trailing)} \quad (6)$$

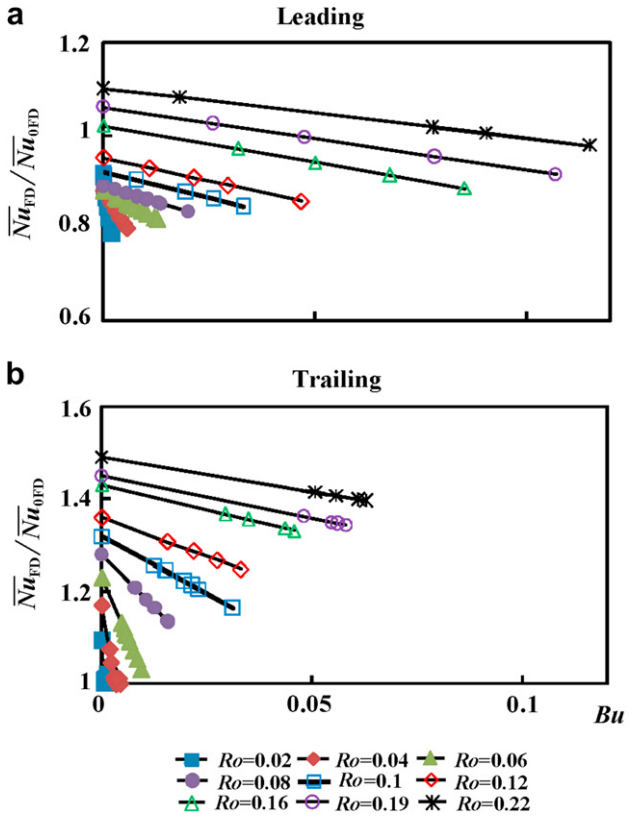

Fig. 12. Variations of $\overline{Nu}_{FD}/\overline{Nu}_{0FD}$ against *Bu* at fixed Ro on (a) leading, (b) trailing wall.

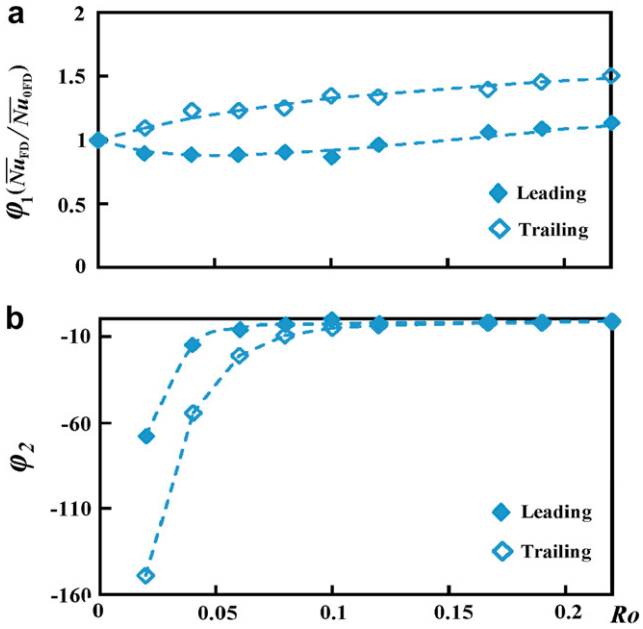

Fig. 13. Variations of (a) φ_1, (b) φ_2 against *Ro*.

Equations (5) and (6) are derived that resolve the uncoupled *Re* and the isolated as well as the interdependent *Ro* and *Bu* effects on $\overline{Nu}_{FD}$ for the developed flow region over the leading and trailing walls of the present rotating wavy channel. This set of $\overline{Nu}_{FD}$ correlation represents all the averaged heat transfer measurements in the developed flow region of the present rotating wavy channel generated by this study. The comparison of all the experimental data with the correlative results calculated by equations (5) and (6) shows the favorable agreements as showed in Fig. 14. There are 95% of $\overline{Nu}_{FD}$ measurements found to be agreed with the correlation results within ±20% discrepancies. Nevertheless, extrapolations of this set of $\overline{Nu}_{FD}$ correlations beyond the parametric ranges specified

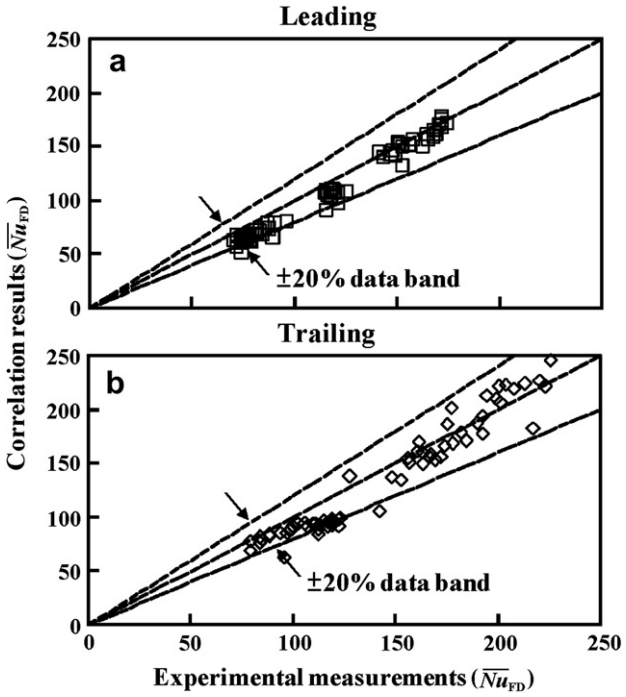

Fig. 14. Comparison of experimental measurements of $\overline{Nu}_{FD}$ over (a) leading, (b) trailing walls with correlation results.

in Table 1 give rise to uncertainties. This study has shown that the present infra-red thermography along with the parametric analysis developed here can provide the detailed *Nu* measurements and correlations for rotating channels with the rotating buoyancy effects examined. Justified by the $\overline{Nu}_{FD}/Nu_\infty$ ratios achieved by employing the skewed wall-waves in the rotating channel, this type of HTE surface has potential applications to the internal coolant channels inside a gas turbine rotor blade.

5. Conclusions

Full-field *Nu* scans are generated by means of the infra-red thermography to permit a detailed examination of both Coriolis and rotating buoyancy effects on the *Nu* distributions over two opposite leading and trailing wavy walls of a radially rotating furrowed channel. Neither any previous study examines the heat transfer performances of the rotating wavy channel, nor can any previously experimental attempt acquire the full *Nu* scans over the rotating surfaces at the pre-defined buoyancy levels. The following salient remarks are disclosed by this study.

1. The cross-plane sectional flows tripped by the skewed wall-waves along with the macro-wall-to-core mixing enhanced by the shear layer instabilities inside the stationary furrowed channel facilitate the considerable HTE effects that respectively elevate $\overline{Nu}_{0FD}/Nu_\infty$ and $\overline{Nu}_0/Nu_\infty$ to 4.57–4.23 and 4.23–4.08 with $4000 \leq Re \leq 14\,000$.
2. Acting by the *Ro* effects alone with diminished buoyancy level, the extrapolated $\overline{Nu}_{FD}/\overline{Nu}_{0FD}$ ratio on the trailing wall increases consistently as *Ro* increases and reaches about 1.5 at $Ro = 0.22$. On the leading wall, the increase of *Ro* from 0 to 0.22 initially reduces the zero-buoyancy $\overline{Nu}_{FD}/\overline{Nu}_{0FD}$ ratios from unity to the worst scenario with the minimum value of about 0.85 at $Ro = 0.04$; beyond which the leading $\overline{Nu}_{FD}/\overline{Nu}_{0FD}$ values are recovered and led to the ratio about 1.1 at $Ro = 0.22$.
3. With the full *Nu* scans collected from the rotational leading and trailing wavy walls, the location dependent heat transfer modifications from the stationary references are disclosed. The trailing *Nu* elevations are triggered from the developed flow region along the obtuse edge and extended in both obtuse-to-acute and upstream directions as *Ro* increases. On the leading wall, the evident *Nu* recovery from the worst heat transfer scenarios at *Ro* above 0.06 also emerges along the obtuse edge of the developed flow region and expands as similar as that on the trailing wall when *Ro* is increased from 0.06 onward.
4. For the present flow configurations and the parametric conditions examined, the rotating buoyancy effects undermine heat transfer performances and are interdependent with *Ro*. Driven by increasing *Bu* at each tested *Ro* for both leading and trailing walls, the low *Nu* regions expand in both acute-to-obtuse and upstream directions with the attendant overall *Nu* reductions over two entire wavy walls. Due to the different *Ro*-driven wave-wise *Nu* variations between leading and trailing walls, the coupling *Ro*–*Bu* impact on $\overline{Nu}_{FD}$ can be correlated by *Ro*, which depicts the weakened *Bu* effect as *Ro* increases from 0 to 0.22.
5. The isolation of *Re* impact from the interdependent *Ro*–*Bu* effects is re-confirmed by normalizing the rotational heat transfer data in terms of Nu/Nu_0 (local basis) or $\overline{Nu}_{FD}/\overline{Nu}_{0FD}$ (area-averaged basis) over the developed flow region. Due to the combined *Ro*–*Bu* impacts with the present parametric conditions, the $\overline{Nu}_{FD}/\overline{Nu}_{0FD}$ ratios fall in the ranges of 0.77–1.03 and 1.02–1.46 on the leading and trailing walls respectively.
6. A set of $\overline{Nu}_{FD}$ correlations that permits the evaluation of the area-averaged *Nu* over the developed flow region on the rotational leading and trailing wavy walls of the furrowed channel is derived to represent the experimental heat transfer data generated by this study with the individual and interdependent influences of *Re*, *Ro* and *Bu* on $\overline{Nu}_{FD}$ to be assessed.

Acknowledgement

This research project was financially sponsored by National Science Council, Taiwan, under the grant number NSC 96-2221-E-022-015MY3.

References

[1] W.D. Morris, S.P. Harasgama, The influence of rotation on the heat transfer characteristics of circular, triangular and square-sectioned coolant passages of gas turbine rotor blades. ASME J. Turbomach. 110 (1988) 44–50.
[2] M.E. Taslim, L.A. Bondi, D.M. Kercher, An experimental investigation of heat transfer in an orthogonally rotating channel roughened with 45° criss-cross ribs on two opposite walls. ASME J. Turbomach. 113 (1991) 346–353.
[3] B.V. Johnson, J.H. Wagner, G.D. Steuber, F.C. Yeh, Heat transfer in rotating serpentine passages with trip skewed to the flow. ASME J. Turbomach. 116 (1994) 113–123.
[4] J.A. Parson, J.C. Han, Y.M. Zhang, Effects of model orientation and wall heating condition on local heat transfer in a rotating two-pass square channel with rib turbulators. Int. J. Heat Mass Transf. 38 (1995) 1151–1159.
[5] L. Al-Hadhrami, J.C. Han, Effect of rotation on heat transfer in two-pass square channels with five different orientations of 45° angled rib turbulators. Int. J. Heat Mass Transf. 46 (2002) 653–669.
[6] T.S. Griffith, L. Al-Hadhrami, J.C. Han, Heat transfer in rotating rectangular cooling channels (AR = 4) with dimples. ASME J. Turbomach. 125 (2003) 555–563.
[7] F.T. Willett, A.E. Bergles, Heat transfer in rotating narrow rectangular pin-fin ducts. Exp. Therm. Fluid Sci. 25 (2002) 573–582.
[8] H. Iacovides, D.C. Jackson, G. Kelemenis, B.E. Launder, Y.-M. Yuan, Flow and heat transfer in a rotating U-bend with 45° ribs. Int. J. Heat Fluid Flow 22 (2001) 308–314.
[9] H. Iacovides, B.E. Launder, Internal blade cooling: the Cinderella of computational and experimental fluid dynamics research in gas turbines. Proc. IMechE A J. Power Energy 221 (2006) 265–290.
[10] S.W. Chang, T.-M. Liou, W.-H. Yeh, J.-H. Hung, Heat transfer in a radially rotating square-sectioned duct with two opposite walls roughened by 45 degree staggered ribs at high rotation numbers. ASME J. Heat Transf. 129 (2007) 188–199.
[11] G. Cardone, T. Astarita, G.M. Carlomagno, Wall heat transfer in static and rotating 180° turn channels by quantitative infrared thermography. Rev. Cén. Therm. 37 (1998) 644–652.
[12] S.W. Chang, T.-M. Liou, T.L. Yang, G.F. Hong, Heat transfer in radially rotating pin-fin channel at high rotation numbers, GT2008–50514, Proceedings of GT2008, ASME Turbo Expo 2008: Power for Land, Sea and Air Conference, Berlin.
[13] K.M. Kim, Y.Y. Kim, D.H. Lee, D.H. Rhee, H.H. Cho, Influence of duct aspect ratio on heat/mass transfer in coolant passages with rotation. Int. J. Heat Fluid Flow 28 (2007) 357–373.
[14] D.K. Lezius, J.P. Johnston, Roll-cell instabilities in rotating laminar and turbulent channel flows. J. Fluid Mech. 77 (1976) 153–175.
[15] R. Kristoffersen, H.I. Anderson, Direct simulation of low-Reynolds number turbulent flow in a rotating channel. J. Fluid Mech. 235 (1993) 163–197.
[16] U. Piomelli, J.H. Liu, Large-eddy simulation of rotating channel flows using a localized dynamic model. Phys. Fluids 7 (1995) 839–848.
[17] A.K. Sleiti, J.S. Kapat, Effects of Coriolis and centrifugal forces on turbulence and transport at high rotation and density ratios in a rib-roughened channel. Int. J. Therm. Sci. 47 (2008) 609–619.
[18] W.D. Morris, T. Aythan, Observations on the influences of rotation on heat transfer in the coolant channels of gas turbine rotor blades. Proc. Inst. Mech. Eng. 193 (1979) 303–311.
[19] J.H. Wagner, B.V. Johnson, B.A. Graziani, F.C. Yeh, Heat transfer in rotating serpentine passages with trips normal to the flow. ASME J. Turbomach. 114 (1992) 847–857.
[20] K.M. Iskakov, V.A. Trushin, The effect of rotation on heat transfer in the radial cooling channels of turbine blades. Teploenergetika 32 (1985) 52–55.
[21] A. Murata, S. Mochizuki, Effect of centrifugal buoyancy on turbulent heat transfer in an orthogonally rotating square duct with transverse or angled rib turbulators. Int. J. Heat Mass Transf. 44 (2001) 2739–2750.
[22] A. Murata, S. Mochizuki, Centrifugal buoyancy effect on turbulent heat transfer in a rotating two-pass smooth square channel with sharp 180-deg turns. Int. J. Heat Mass Transf. 47 (2004) 3215–3231.
[23] S.W. Chang, W.D. Morris, A comparative study of heat transfer between rotating circular smooth-walled and square rib-roughened ducts with cooling application for gas turbine rotor blades. JSME Int. J. Ser. B 41 (1998) 302–315.

[24] S.W. Chang, T.L. Yang, T.-M. Liou, G.F. Hong, Heat transfer in rotating scale-roughened trapezoidal duct at high rotation numbers. J. Appl. Therm. Eng. 29 (2009) 1682–1693.
[25] S.W. Chang, T.L. Yang, T.-M. Liou, G.F. Hong, Heat transfer of rotating rectangular duct with compound scaled roughness and V-ribs at high rotation numbers. Int. J. Therm. Sci. 48 (2009) 174–187.
[26] S.W. Chang, T.-M. Liou, K.F. Chiang, G.F. Hong, Heat transfer and pressure drop in rectangular channel with compound roughness of V-shaped ribs and deepened scales. Int. J. Heat Mass Transf. 51 (2008) 457–468.
[27] M. Ali, S. Ramadhyani, Experiments on convective heat transfer in corrugated channels. Exp. Heat Transf. 5 (1992) 175–193.
[28] T. Nishimura, A. Tarumoto, Y. Kawamura, Flow and mass transfer characteristics in wavy channels for oscillatory flow. Int. J. Heat Mass Transf. 31 (1987) 1007–1015.
[29] T.A. Rush, T.A. Newell, A.M. Jacobi, An experimental study of flow and heat transfer in sinusoidal wavy passages. Int. J. Heat Mass Transf. 42 (1999) 1541–1553.
[30] S.W. Chang, A.W. Lees, T.S. Chou, Heat transfer and pressure drop in furrowed channels with transverse and skewed sinusoidal wavy walls. Int. J. Heat Mass Transf. 52 (2009) 4592–4603.
[31] H. Iacovides, D.C. Jackson, G. Kelemenis, B.E. Launder, Y.M. Yuan, Experiments on local heat transfer in a rotating square-ended U-bend. Int. J. Heat Fluid Flow 20 (1999) 302–310.
[32] Y. Eto, S. Obi, S. Masuda, Heat transfer experiments in rotating boundary layer flow. Int. J. Heat Fluid Flow 21 (2000) 684–692.
[33] JHT Editorial Board of ASME J. Heat Transfer, Journal of heat transfer policy on reporting uncertainties in experimental measurements and results. ASME J. Heat Transf. 115 (1993) 5–6.
[34] S.W. Chang, L.M. Su, T.L. Yang, S.F. Chiou, Enhanced heat transfer of forced convective fin flow with transverse ribs. Int. J. Therm. Sci. 43 (2004) 185–200.
[35] G. Russ, H. Beer, Heat transfer and flow field in a pipe with sinusoidal wavy surface – I. Numerical investigation. Int. J. Heat Mass Transf. 40 (1997) 1061–1070.